SpezialForschungsBereich F 32

Karl–Franzens Universität Graz
Technische Universität Graz
Medizinische Universität Graz

Optimum Receiver Array Design for Magnetic Induction Tomography

Doğa Gürsoy Hermann Scharfetter

SFB-Report No. 2008–010 September 2008

A–8010 GRAZ, HEINRICHSTRASSE 36, AUSTRIA

Supported by the
Austrian Science Fund (FWF)

Der Wissenschaftsfonds.

SFB sponsors:

- **Austrian Science Fund** (FWF)
- **University of Graz**
- **Graz University of Technology**
- **Medical University of Graz**
- **Government of Styria**
- **City of Graz**

Optimum Receiver Array Design for Magnetic Induction Tomography

Doğa Gürsoy and Hermann Scharfetter

September 1, 2008

Abstract

Magnetic Induction Tomography (MIT) is an imaging modality which aims at mapping the distribution of the electrical conductivity inside the body. Eddy currents are induced in the body by magnetic induction and the resulting fields are measured by an array of receiver coils. In MIT, the location of the receivers affects the quality of the image reconstruction. In this paper, a fast deterministic algorithm was applied to obtain optimum receiver array designs for a given specific excitation. The design strategy is based on the iterative exclusion of receiver locations, which yield poor conductivity information, from the space spanning all possible locations until a feasible design is reached. The applicability of "regionally focused" MIT designs which increase the image resolution at a particular region was demonstrated. Currently used design geometries and the corresponding reconstructed images were compared to the images obtained by optimized designs. The eigenvalue analysis of the Hessian matrix showed that the algorithm tends to maintain identical conductivity information content sensed by the receivers. Although the method does not guarantee finding the optimum design globally, the results demonstrate the practical usability of this algorithm in MIT experimental designs.

Keywords: Magnetic induction tomography, optimum design, information measure

1 Introduction

MIT is an imaging modality which aims to reconstruct the interior conductivity distribution of the body [1]–[7]. The body is exposed to alternating magnetic fields by an array of transmitter coils which induces eddy currents in the tissues. These currents generate their own secondary magnetic field which, in principle,

[1]D. Gürsoy and H. Scharfetter are with the Institute of Medical Engineering, Graz University of Technology, Austria. e-mail: guersoy@tugraz.at

[2]This work was supported by the SFB project F32-N18 granted by the Austrian Science Fund and published in IEEE Trans. Biomed. Eng.

contains information about the conductivity distribution inside the body. However, the secondary fields are much weaker than the main excitation field, thus, the cancellation of the main excitation is essential to increase the dynamic range of the receiver channels. Usually, flux cancellation techniques like back off coils [4], specially oriented coils [8]–[11] and gradiometers realized on PCB [5] or as coils [7] have been used for this purpose. Therefore, the measured data are essentially the voltages induced in the receiver coils by the secondary magnetic field.

In practice, because of the nonlinear relation between the MIT measurements and the conductivity of the body, the variations in measurements caused by small conductivity changes around a linearized forward operator (the Jacobian of the forward operator calculated at a specific conductivity distribution) have commonly been used to reconstruct images [12]–[15]. Usually, a uniform phantom is used to calculate the Jacobian, however, nonuniform phantoms may also be used. Similarly, in this paper, the forward operator was assumed to be linear around an acceptable region of uniform body conductivity distribution.

Several experimental MIT systems have been built [3]–[5]. Most of them are designed to encircle the body on a transverse plane and have 8 or 16 measurement channels. The excitation by coils causes a diffuse field which consequently results in poor image resolution. Although an increase in the number of transmitters and receivers theoretically provides more information, the quality of the images does not improve significantly beyond a certain number because of increasing correlation between the individual data. Additionally, the maximum number of coils for both excitation and detection is physically constrained unless a scanning protocol including coil movements is applied.

In this paper, it is aimed to obtain optimum locations of the receiver coils given a specific excitation geometry. The applied algorithm was previously suggested to increase data information for seismic and geophysical surveys [16]. The quality measure of the receiver geometries was computed based on the mutual information content between the measurements. A similar approach for the quantification of the overall data quality have recently been offered for electrical impedance tomography (EIT) [17]. The design strategy used in this paper aims at iteratively excluding such arrangements, which has the most correlated conductivity information from the space spanning all possible arrangements until a stopping criterion is reached. The method does not guarantee finding the global optimum, however, a close approximation is possible by a good initial discretization of the receiver geometry. The algorithm is also capable of finding a design which focuses onto a region inside the body so as to increase the image resolution at that region.

2 Methods

2.1 Forward problem

The relation of the voltage data and the electrical properties is expressed as,

$$v = \psi(\kappa, \zeta) \tag{1}$$

where ψ is a nonlinear operator acting on the given distribution of electrical properties ($\kappa = \sigma + jw\epsilon$) for a given sensor positioning (ζ).

To simulate the voltages, the fields in the body should be solved given the applied primary magnetic potential by the transmitter coils. For medical applications of MIT, it is usually assumed that the contribution of the induced currents to the primary magnetic potential to be negligible. This results in decoupling of the field equations [18]. Therefore, the magnetic potential distribution calculated [19] in the absence of a conducting body is used for the solution of the electric potential. The resulting partial differential equations for the solution of the scalar potential in the body are given as follows,

$$\nabla \cdot \kappa \nabla \phi = -jw\mathbf{A} \cdot \nabla \kappa \tag{2}$$

$$\frac{\partial \phi}{\partial n} = -jw\mathbf{A} \cdot \mathbf{n} \tag{3}$$

where w is the operating frequency of the excitation field, ϕ and $\mathbf{A}$ are the electric scalar potential and magnetic vector potential, respectively, and $\mathbf{n}$ is the normal vector directed outward from the body surface. The equation set was discretized by the Finite Element Method and solved by the inverse based multilevel preconditioned quasi minimum residual method [20]. Using the solved potentials, the electric field in the body was found by,

$$\mathbf{E} = -\nabla \phi - jw\mathbf{A} \tag{4}$$

The electric field in the body generates a secondary magnetic field which was calculated from the Biot-Savart law,

$$\mathbf{B} = \frac{\mu_0}{4\pi} \int \kappa \mathbf{E} \times \frac{\mathbf{r}}{r^3} \, dV \tag{5}$$

where $\mathbf{r}$ is the displacement vector in the direction pointing from the element towards the point at which the field is being computed and the integration is taken over the volume of the body. In MIT, the measured quantity is the voltages induced in the receiving coils because of the existing magnetic field. The voltage signal can be subdivided into two parts due to the influence by the primary and the secondary magnetic field. The first one is independent of the electrical properties and the cancellation of that signal from the data is usually desired. Possible ways of cancellation are using gradiometers, back off coils or lateral positioning of receivers. In this paper, it was assumed that a perfect cancellation of the primary signal was established. Therefore the

induced secondary voltages in the receiver coils were found using Lenz's Law by integrating the magnetic field over the receiver coil surfaces,

$$v = -jw \int \mathbf{B} \cdot d\mathbf{S} \tag{6}$$

The real part of the voltage data (in-phase component with respect to the primary excitation) contains conductivity information and the imaginary part contains the permittivity information of the body. Usually the imaginary component is much more noisier due to technical reasons [21] which makes permittivity imaging very challenging. In this paper imaging of the conductivity distribution is desired, therefore, only the real component was used.

2.2 Inverse problem

Although ψ is a nonlinear function, usually a linearization of this operator is possible around a given σ_o assuming σ_o is in the close vicinity of the expected body parameters. This linear relation is expressed as,

$$\frac{\partial \psi(\sigma_o)}{\partial \sigma} \Delta\sigma = \Delta v \tag{7}$$

In the context of MIT, the Jacobian of the forward operator at a given conductivity distribution is usually named the sensitivity and the discretisized linear relationship assuming piecewise constant conductivity distribution is written as follows,

$$\mathbf{S}_o \Delta\sigma = \Delta v \tag{8}$$

where $\mathbf{S}_o$ is called the sensitivity matrix for a given σ_o. The sensitivity matrix was calculated by using the generalized version of Geselowitz's relationship [22] which is based on the reciprocity theorem and generally used for sensitivity calculations in EIT. It is defined as,

$$\mathbf{s}_k = \int \Delta\sigma \mathbf{E}_i \cdot \mathbf{E}_j \; dV \qquad k = 1, 2, .., n \tag{9}$$

where $\mathbf{E}_i$ and $\mathbf{E}_j$ are the electric fields created in the body by the normal and adjoint excitations of the transmitter and receiver coils, respectively, and n is the number of independent transmit-receive combinations. s_k denotes the k^{th} row of the sensitivity matrix.

The inverse problem is usually ill-posed and needs regularization in the presence of data inaccuracies. The strong numerical singularity arises because of the fact that some of the eigenvalues of the Hessian of the forward operator are very small which causes a strong amplification of the errors in the conductivity domain. The reconstruction method used for imaging uses a single step regularized Gauss-Newton iteration as follows,

$$\Delta\sigma = (\mathbf{S}_o^T \mathbf{S}_o + \lambda \mathbf{R})^{-1} \mathbf{S}_o^T \Delta v \tag{10}$$

where $\mathbf{S}_o^T\mathbf{S}_o$ is an approximation of the Hessian for a given σ_o, $\mathbf{R}$ is the regularization matrix and λ is the regularization parameter. In this study $\mathbf{R}$ was chosen as the identity matrix and λ was obtained according to the Morozov criterion [23].

2.3 Optimization algorithm

The design strategy used in this paper aims at maximizing the degree of the independence between the rows of the sensitivity matrix in order to decrease the condition number of the Hessian matrix. The quality measure for a particular design is defined in terms of the N-dimensional angle between the rows of the sensitivity matrix as given below,

$$\alpha_{mn} = \left(\frac{\mathbf{s}_m \cdot \mathbf{s}_n}{\|\mathbf{s}_m\| \, \|\mathbf{s}_n\|} \right)^2 \tag{11}$$

where $\mathbf{s}_i$ corresponds to the i^{th} row of the sensitivity matrix. The α values are simply the square of the cosines of the angles between the rows and are defined in $[0, 1]$. This relationship is sometimes referred to as the normalized data resolution (or information) matrix. The more orthogonal the vectors are, the more independent information content they provide. Similarly, a quality measure for a specific receiver (see Appendix) is given as follows,

$$Q_r = \frac{1}{KN} \sum_{k=1}^{K} \sum_{n=1}^{N} (1 - \alpha_{kn}) \tag{12}$$

Here N is the possible number of independent measurements (total number of rows in the sensitivity matrix) and K is the number of different transmitters which yield the different measurements in the k^{th} receiver. Q_r reflects the gain of information which each receiver contributes to the information of the whole set.

Usually the maximization of the resolution in a particular region (e.g. a slice) is desired . This is possible by weighting the sensitivity matrix before the optimization procedure by multiplying all the columns of the sensitivity matrix with weights in such a way that columns corresponding to voxels in the focus region are emphasized while the remaining ones are de-emphasized. In the extreme case all the columns of the sensitivity matrix for voxels outside the focus region are set to zero.

The applied algorithm works as follows: (1) Choose a set of receiver geometries that spans all feasible designs in a discrete manner, (2) compute the sensitivity of the whole set. If focusing to a specific region is desired, use the weighted sensitivity matrix. (3) compute the angles between all rows associated with independent transmit-receive combinations, (4) reduce the receiver which provides the least loss of information when being removed from the remaining set. (5) Update the sensitivity matrix by deleting the rows corresponding to the discarded receiver. (6) Continue looping through these steps (2-5) until a

stopping criterion is reached. In this paper, the algorithm was stopped when a desired number of receivers, i.e. 16 or 32 was reached. Of course other criteria are possible, i.e. until the achievable resolution in a certain region passes a certain threshold or the algorithm could also stop if the derivative of the overall quality measure calculated at each step exceeds a certain threshold.

2.4 Evaluation of resulting designs

For the evaluation, the eigenvalue spectrum of the Hessian matrix is investigated. From matrix algebra it is known that,

$$trace(\mathbf{S}^T\mathbf{S}) = \sum_m \lambda_m \tag{13}$$

where λ_m is the m^{th} eigenvalue of the Hessian matirx ($\mathbf{S}^T\mathbf{S}$). The trace of the Hessian matrix as a measure of the resolution (e.g. see [24]) was used to demonstrate the improvements of the resulting designs. When focusing into a region is desired, the weighted sensitivity matrix was used for the analysis.

2.5 Model

A cylindrical phantom (0.1 S/m) which has 3 local spherical inhomogeneities (0.2 S/m) was used for simulations (as in Figure 1). The phantom had a radius of 100 mm and a height of 300 mm. Each inhomogeneity had a radius of 10 mm and was positioned at (60, 0, 50), (-60, 0, 0) and (30, 0, -70) mm. The voltage data was simulated by changing the conductivity of the perturbations from 0.1 S/m to 0.2 S/m. The permittivity was kept constant with 80 in the whole phantom. The tetrahedral mesh was created with the commercial software HyperMesh (Altair Inc.). The total element number was approximately 100 000 for simulating the data (forward model) and 30 000 for the image reconstructions (inverse model).

Two different transmitter coil arrangements were selected for the simulations (see Figure 1). For convenience they will be referred to as T1 and T2. In T1, 8 uniformly positioned identical and radially oriented transmitters of 40 mm radius encircle the phantom, whereas, in T2, the number of circular transmitters was doubled and they were positioned in a zigzag pattern. The excitation current was 1 A for each transmitter and the excitation frequency was chosen as 200 kHz.

The full starting set of all feasible receiver positions is given in Figure 2. The radius of the receiver coils was chosen as 20 mm and they encircle the phantom in 16 equidistant locations on 7 rings. A total of 112 circular receiver coils was used to initialize the design algorithm.

3 Results

Three different optimization designs were realized for both T1 and T2 according to the desired improvement of the image resolution at different regions of the

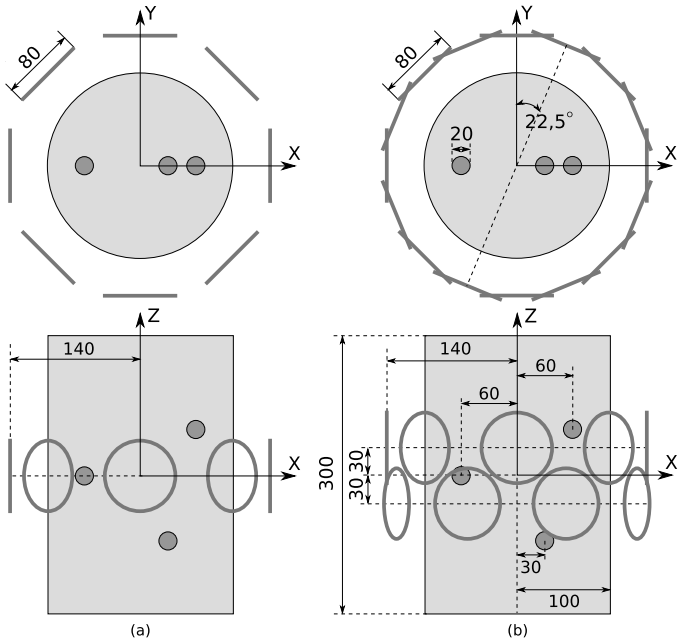

Figure 1: Transmitter arrangements around the cylindrical phantom (0.1 S/m) which has 3 local spherical inhomogeneities (0.2 S/m). (a) 8 flat transmitter coil geometries [T1] and (b) 16 crosswise transmitter coil geometries [T2] were used for excitation. Upper diagrams are the top views and lower ones are the side views of the simulation arrangements. All distance units are in mm.

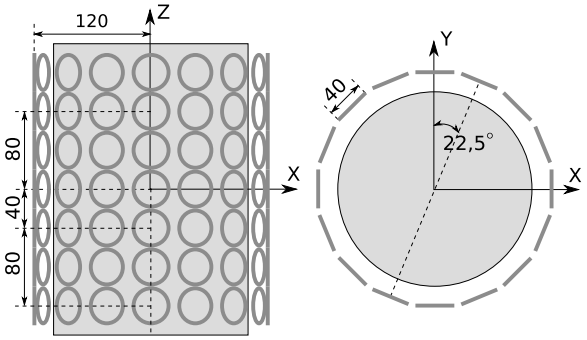

Figure 2: The possible receiver locations selected for the initialization of the design optimization. Left diagram is the side view and right one is the top view.

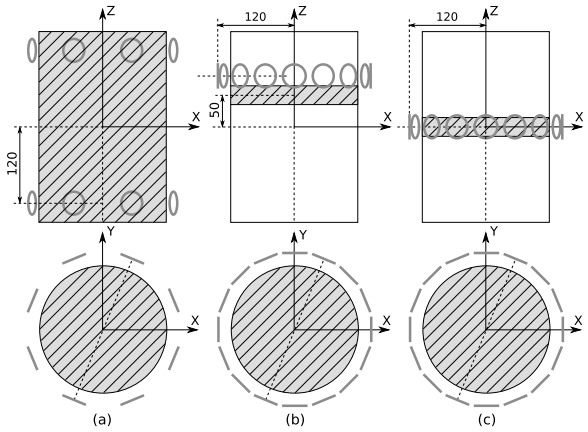

Figure 3: Optimum receiver designs for T1. The dashed area at each phantom represents the region of which the information content is maximized. (a) the design [R1] without focusing. (b) The design [R2] obtained by focusing to the the slice at z = 50 mm. (c) The design [R3] obtained by focusing to the central slice.

phantom. The first design should increase the resolution in the whole phantom and will be referred to as R1. In this case no weighting was applied to the sensitivity matrix. The other two designs should increase the resolution in the transversal slices of 30 mm thickness placed at 50 and 0 mm height on the z-axis and will be referred to as R2 and R3, respectively. In these designs, for proper focusing, all the columns of the sensitivity matrix for voxels outside the focus region are set to zero, whereas, the focused ones were not changed. The resulting optimum designs for the T1 and T2 excitations are given in Figure 3 and 5 respectively. In the figure, the dashed area at each phantom represents the region of which the information content was maximized. In R1, the optimum set of receiver coils forms two rings which are vertically 240 mm apart from each other. However, when a regional focusing was desired, the optimum set of receiver coils encircles a specific region of the selected slice in a single plane. In a second run the same strategy was applied with T2 as the transmit configuration. Similar to R1, R2 and R3, the corresponding designs will be referred to as Ra, Rb, and Rc respectively, depending on the focus region.

When focusing at a certain region the resolution of the images clearly increased when compared to the unfocused case (see Figure 4 and 6 by visual perception and Table 1 quantitatively). However, this local gain of resolution was achieved at the cost of a significant resolution loss outside the focus region. Consequently only in the unfocused versions (R1 and Ra) all three perturbations could be identified simultaneously, while all other designs failed to do so. On the other hand, due to the lack of focusing, the R1 and Ra designs led to more blurry images. The reconstructions of the slice at z = 50 mm were best when using the designs R2 and Rb. However the lower half of the phantom had poor

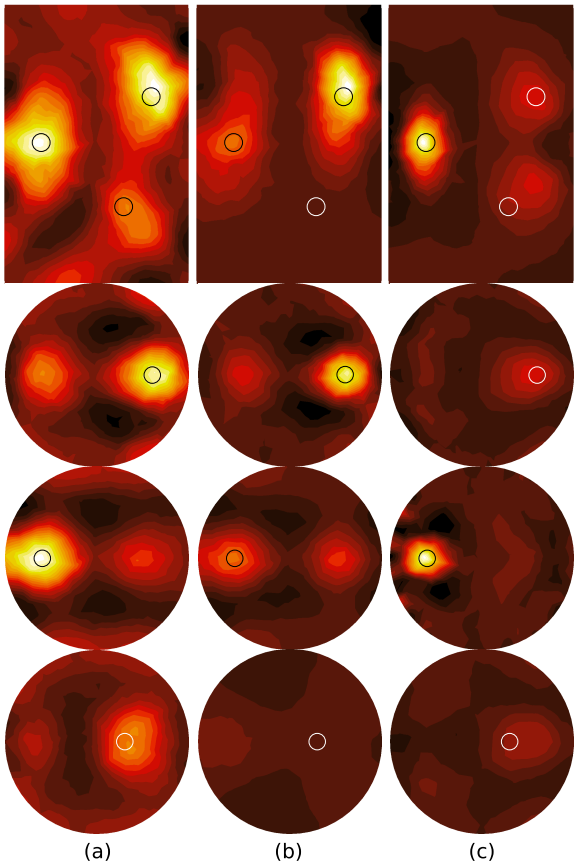

Figure 4: Reconstructions with the optimum receiver designs by using T1 as excitation. (a) the reconstruction obtained using R1 without focusing. (b) The reconstruction obtained using R2 which focuses to the the slice at z = 50 mm. (c) The reconstruction obtained using R3 which focuses to the central slice.

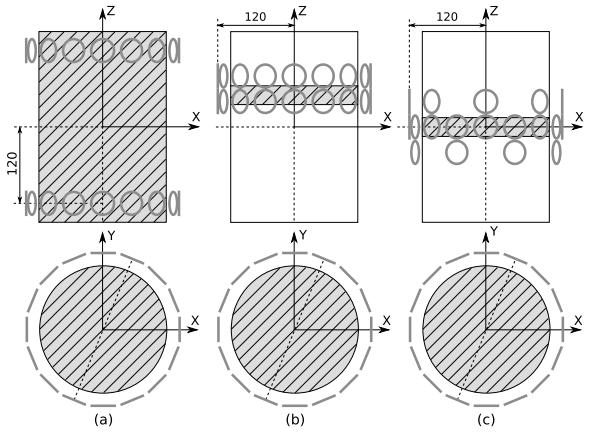

Figure 5: Optimum receiver designs for T2. The dashed area at each phantom represents the region of which the information content is maximized. (a) The design [Ra] without focusing. (b) The design [Rb] obtained by focusing to the the slice at z = 50 mm. (c) The design [Rc] obtained by focusing to the central slice.

resolution. In the design R3, a spurious mirror image of the upper perturbation appeared in the lower half of the cylinder, probably because of the symmetry of the coil arrangement with respect to the median plane. The lower perturbation was possibly cloaked by that mirror artifact, due to the comparatively lower low sensitivity at the respective depth. When the focus should be on the central slice, the algorithm suggests to encircle the phantom with a uniformly distribution of the receiver coils in the central plane of the slice, as seen in R3. Similarly, vertically paired receivers are placed in front of each transmitter coil, see the results for Rb.

The comparisons of the eigenvalues of the Hessian matrix obtained from different transmitter and receiver designs are given in figure 7, 8, and 9. In figure 7, the eigenvalues of the Hessian matrices obtained from T1 as the excitation configuration and R1, R2 and R3 as the optimized receiver designs. As expected, the design R1 tends to flatten the eigenvalue spectrum by increasing the small eigenvalues and reducing the larger ones. In figure 8, the corresponding spectrum was obtained similarly except that the Hessian was calculated only from those columns of the sensitivity matrix the voxels of which correspond to the central slice. It was noticed that the design Rc focusing onto the central slice provided the largest eigenvalues. Figure 9 shows that the design T2-Rc outperforms the design T1-R3 when comparing especially the smaller eigenvalues of the respective eigenvalue spectra. The quantitative results of resolution analysis was given in Table 1. The resolution of the central slice is largest for T1-R3 and T2-Rc design compared to the remaining designs. Similarly T1-R2 and T2-Rb designs have the largest resolution at the slice positioned at z = 50 mm.

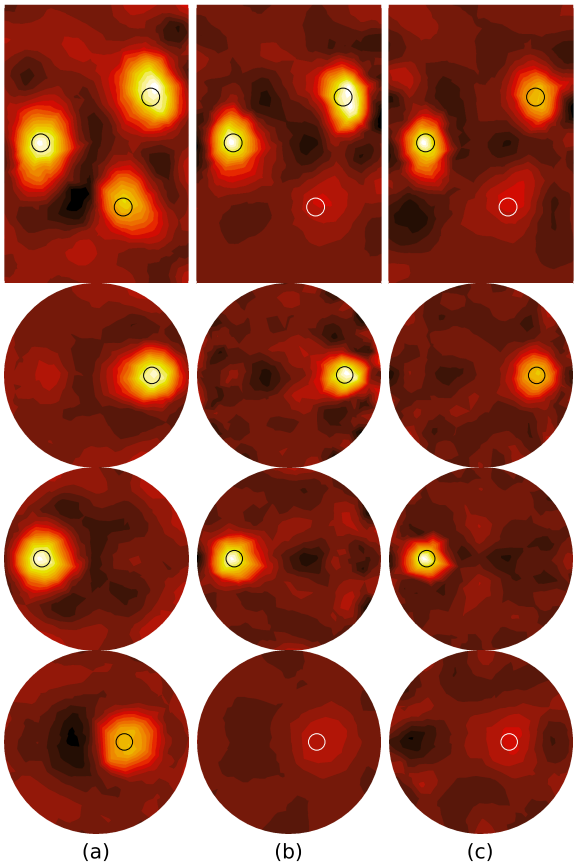

Figure 6: Reconstructions with the optimum receiver designs by using T2 as excitation. (a) the reconstruction obtained using Ra without focusing. (b) The reconstruction obtained using Rb which focuses to the the slice at z = 50 mm. (c) The reconstruction obtained using Rc which focuses to the central slice.

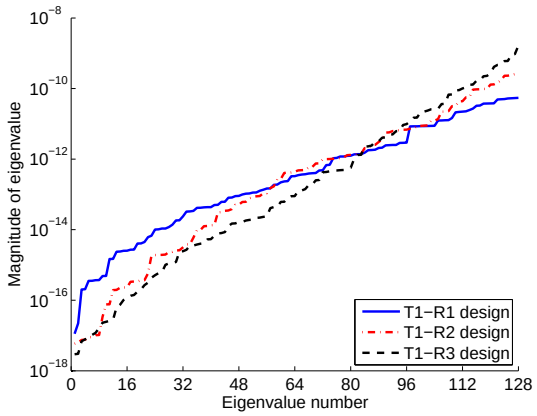

Figure 7: The corresponding eigenvalues of the Hessian matrices obtained from R1, R2 and R3 as receiver designs and T1 as the excitation scheme.

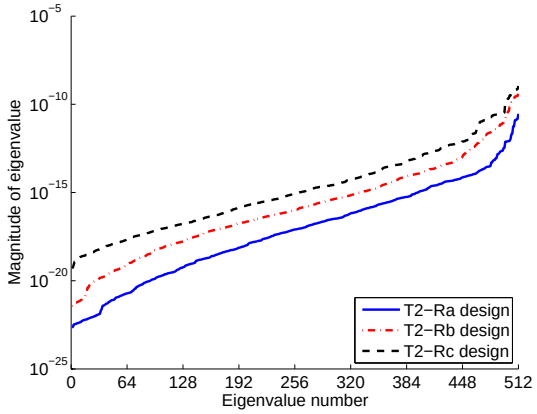

Figure 8: The eigenvalues of the Hessian matrices obtained from Ra, Rb and Rc as receiver designs and T2 as the excitation scheme. Only the coloumns of the sensitivity matrix which corresponds to the central slice were used for the calculation of the Hessian.

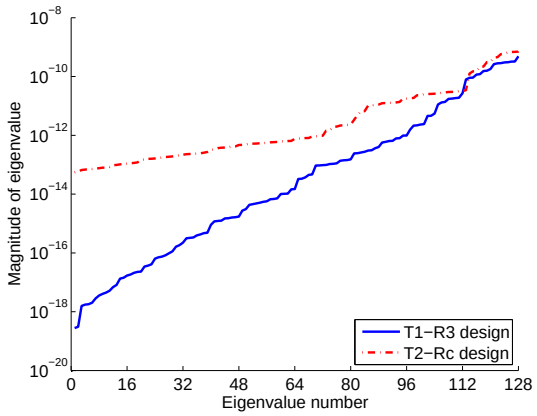

Figure 9: The corresponding eigenvalues of the Hessian matrices obtained from R1 and Ra as receiver designs and T1 and T2 as the excitation schemes. For convenience, only the largest 128 of 512 eigenvalues are plotted for T2-Rc design.

Table 1: Total resolution ($trace(\mathbf{S}^T\mathbf{S})$) of (A) the central slice and (B) the slice at z = 50 mm for the corresponding designs.

	(A)	(B)
$T1-R1$	$0.018 \cdot 10^{-9}$	$0.109 \cdot 10^{-9}$
$T1-R2$	$0.170 \cdot 10^{-9}$	$1.210 \cdot 10^{-9}$
$T1-R3$	$3.730 \cdot 10^{-9}$	$0.743 \cdot 10^{-9}$
$T2-Ra$	$0.106 \cdot 10^{-9}$	$0.341 \cdot 10^{-9}$
$T2-Rb$	$2.691 \cdot 10^{-9}$	$6.184 \cdot 10^{-9}$
$T2-Rc$	$8.071 \cdot 10^{-9}$	$3.425 \cdot 10^{-9}$

4 Discussions

In this paper, the forward operator of MIT was linearized around a given conductivity distribution and small variations between different conductivity states were reconstructed according to the idea of difference imaging. This linearization renders possible the use of a deterministic approach. The design strategy developed was based on the calculation of the sensitivity matrix. Therefore no voltage data simulation or noise considerations were needed to obtain optimal designs. MIT designs which are currently used in existing hardware were evaluated and it was shown that better designs can be achieved for different excitation and receiver patterns.

The solution of the inverse problem is a time consuming process. Even in the linearized case, the optimum experimental design approaches requires a vast number of forward problem solutions. Thus, it is essential to reduce the possible set of solutions to a computationally feasible set. The resulting designs are, accordingly, assumed to be an optimum subset of the initial set of geometries. This method does not guarantee the global optimum because of the practical infeasibility of evaluating all possible combinations of the whole set. However, the results showed that it is possible to find an optimal setup for some practical experiments.

The possibility of "regionally focused" MIT was demonstrated. This strategy increases the image resolution in a particular region at the cost of other regions' resolution. As to the knowledge of the authors, designs which focus on a specific slice have not yet been described quantitatively in much detail. The reason may be that intuition suggests to place the receivers on a ring encircling the body on a transverse plane as closely as possible to the slice which should be investigated. This assumption is possibly the heritage of the 2D EIT imaging and was taken as a standard for MIT designs. Although it was previously found that the resolution near the receivers is higher compared to far regions, it is unclear whether the currently used designs focus on a particular region or not.

When the increase in the resolution of the central slice is desired, the optimal receiver locations which were suggested by our algorithm are intuitive in that sense that they lead to a concentration of coils close to the desired slice of the body with a fairly equidistant spacing. However the more the desired slice is far away from the transmitter plane, the receiver locations are not chosen as the closest locations to that slice, but, a bit in opposite direction with respect to transmitter plane (i.e. see figure 3-b). In addition, the results also clearly emphasize the poor resolution in regions outside the focus volume. It was also noted that the solutions with a fair overall resolution cannot be found unless the coils are also spread over a wider range in the z-direction.

5 Appendices

5.1 Optimization measure

In information theory, the mutual information of two random variables is a quantity that measures the mutual dependence of the two variables and will provide a basis for the optimization. Let $\mathbf{d} = [d_1, d_2]$ is the data vector consisting two channels and have a multivariate normal distribution with mean vector μ_d and covariance matrix $\mathbf{C}_d$. If the covariance matrix of the model parameters is assumed to be an identity matrix then,

$$\mathbf{C}_d = \mathbf{S}\mathbf{S}^T = \begin{bmatrix} (\mathbf{s}_1 \cdot \mathbf{s}_1) & (\mathbf{s}_1 \cdot \mathbf{s}_2) \\ (\mathbf{s}_1 \cdot \mathbf{s}_2) & (\mathbf{s}_2 \cdot \mathbf{s}_2) \end{bmatrix} \tag{14}$$

The mutual information between these two data [25] is,

$$I(d_1; d_2) = H(d_1) + H(d_2) - H(d_1, d_2) \tag{15}$$

$$= -\frac{1}{2} log \left(1 - \frac{(\mathbf{s}_1 \cdot \mathbf{s}_2)^2}{(\mathbf{s}_1 \cdot \mathbf{s}_1)(\mathbf{s}_2 \cdot \mathbf{s}_2)} \right) \tag{16}$$

By noting that $(\mathbf{s}_1 \cdot \mathbf{s}_2)^2/(\mathbf{s}_1 \cdot \mathbf{s}_1)(\mathbf{s}_2 \cdot \mathbf{s}_2) \in [0, 1]$, minimizing the mutual information between two data can be equivalently established by maximizing the following function,

$$q_{12} = 1 - \left(\frac{\mathbf{s}_1 \cdot \mathbf{s}_2}{\|\mathbf{s}_1\| \, \|\mathbf{s}_2\|} \right)^2 \tag{17}$$

where q can be defined as a quality measure between the two data. Let there are N independent data and K different transmitters influencing a single receiver, then, the average quality for that receiver is written as,

$$Q_r = \frac{1}{KN} \sum_{k=1}^{K} \sum_{n=1}^{N} q_{kn} \tag{18}$$

Acknowledgments

The authors thank Olaf Steinbach, Institute of Numerical Mathematics, Graz University of Technology, as the main partner concerning mathematical issues within the subproject. This cooperation and many fruitful discussions with Manuel Freiberger, Sarah Engleder and Sabine Zaglmayr are gratefully acknowledged.

References

[1] A. Peyton, "An overview of electromagnetic inductance tomography: description of three different systems," *Meas. Sci. Technol.*, vol. 7, pp. 261-71, 1996.

[2] A. V. Korjenevsky and V. A. Cherepenin, "Progress in realization of magnetic induction tomography," *Ann. N Y Acad. of Sci.*, vol. 873, pp. 346-52, 1999.

[3] A. Korjenevsky, V. Cherepenin and S. Sapetsky, "Magnetic induction tomography: experimental realization," *Physiol. Meas.*, vol. 21, pp. 88-94, 2000.

[4] H. Griffiths, W. R. Stewart, and W. Gough, Magnetic induction tomography. a measuring system for biological tissues," *Ann. N Y Acad. Sci.*, vol. 873, pp. 335-45, 1999.

[5] H. Scharfetter, H. Lackner, and J. Rosell, "Magnetic induction tomography: Hardware for multi-frequency measurements in biological tissues," *Physiol. Meas.*, vol. 22, pp. 131-46, 2001.

[6] H. Griffiths, "Magnetic Induction Tomography," *Meas. Sci. Technol.*, vol. 26, pp. 1126-31, 2001.

[7] B. U. Karbeyaz and N. G. Gençer, "Electrical conductivity imaging via contactless measurements: an experimental study," *IEEE Trans. Med. Imag.*, vol. 22, pp. 627-35, 2003.

[8] C. H. Igney, S. Watson, R. J. Williams, H. Griffiths, O. Dossel, "Design and performance of a planar-array MIT system with normal sensor alignment," *Physiol. Meas.*, vol. 26, pp. 263-78, 2005.

[9] S. Watson, A. Morris, R. J. Williams, H. Griffiths and W. Gough, "A primary field compensation scheme for planar array magnetic induction tomography," *Physiol. Meas.*, vol. 25, pp. 271-9, 2004.

[10] S. Watson, C. H. Igney, O. Dossel, R. J. Williams and H. Griffiths, "A comparison of sensors for minimizing the primary signal in planar-array magnetic induction tomography," *Physiol. Meas.*, vol. 26, pp. 319-31, 2005.

[11] H. Scharfetter, R. Merwa and K. Pilz, "A new type of gradiometer for the receiving circuit of magnetic induction tomography (MIT)," *Physiol. Meas.*, vol. 26, pp. 307-18, 2005.

[12] R. Merwa, K. Hollaus, P. Brunner and H. Scharfetter, "Solution of the inverse problem of magnetic induction tomography (MIT)," *Physiol. Meas.*, vol. 26, pp. 241-50, 2005.

[13] H. Scharfetter, S. Rauchenzauner, R. Merwa, O. Biro and K. Hollaus, "Planar gradiometer for magnetic induction tomography (MIT): Theoretical and experimental sensitivity maps for a low-contrast phantom," *Physiol. Meas.*, vol. 25, pp. 325-33, 2004.

[14] P. Brunner, R. Merwa, A. Missner, J. Rosell, K. Hollaus and H. Scharfetter, "Reconstruction of the shape of conductivity spectra using differential multi-frequency magnetic induction tomography," *Physiol. Meas.*, vol. 27, pp. 237-48, 2006.

[15] N. G. Gençer and M. N Tek, "Electrical conductivity imaging via contactless measurements," *IEEE Trans. Med. Imag.*, vol. 18, pp. 617-27, 1999.

[16] A. Curtis, A. Michelini, D. Leslie and A. Lomax, "A deterministic algorithm for experimental design applied to tomographic and microseismic monitoring surveys," *Geophys. J. Int.*, vol. 157, pp. 595-606, 2004.

[17] A. Adler, R. Youmaran, W. R. B. Lionheart, "A measure of the information content of EIT data ," *Physiol. Meas.*, vol. 29, pp. 101-9, 2008.

[18] N. G. Gençer and M. N. Tek, "Forward problem solution for electrical conductivity imaging via contactless measurements," *Phys. Med. Biol.*, vol. 44, pp. 927-40, 1999.

[19] W. R. Smythe, *Static and dynamic electricity*, New York: McGraw Hill, pp. 290-1, 1965.

[20] L. Horesh, M. Schweiger, M. Bollhofer, A. Douiri, D. S. Holder and S. R. Arridge, "Multilevel preconditioning for 3D large scale soft field medical applications modeling," *Int. J. Inf. Syst. Sci.*, vol. 2, pp. 532-56, 2006.

[21] H. Scharfetter, R. Casaas and J. Rosell, "Biological Tissue Characterization by Magnetic Induction Spectroscopy (MIS): Requirements and Limitations," *IEEE Trans. Biomed. Eng.*, vol. 50, pp. 870-80, 2003.

[22] J. R. Mortarelli, "A Generalization of the Geselowitz Relationship Useful in Impedance Plethysmographic Field Calculations," *IEEE Trans. Biomed. Eng.*, vol. 27, pp. 665-7, 1980.

[23] P. Hansen, *Rank-Deficient and Discrete Ill-Posed Problems,* Philadelphia: SIAM, 1998.

[24] A. Curtis, "Optimal designs of focused experiments and surveys," *Geophys. J. Int.*, vol. 139, pp. 205-15, 1999.

[25] T. M. Cover, J. A. Thomas, *Elements of Information Theory*, New York: Wiley, 2006.